The high-pressure electronic spin transition in iron: Potential impacts upon mantle mixing

M. H. Shahnas,[1] W. R. Peltier,[1] Z. Wu,[2] and R. Wentzcovitch[3]

Received 1 September 2010; revised 1 May 2011; accepted 18 May 2011; published 9 August 2011.

[1] At the Rayleigh number appropriate to Earth's mantle, radial heat transport is dominated by solid state thermal convection. Because of the large number of physical properties required to determine the Rayleigh number, and because these properties are expected to be (perhaps strong) functions of pressure and temperature (P-T), laboratory measurements of them under the high pressure and temperature conditions that occur in the deep Earth are of fundamental importance. Recent experimental data demonstrate that an electronic spin transition in iron that occurs at midmantle depths results in significant changes in the physical properties of the ferropericlase component of mantle mineralogy. Additional recent results suggest that it may also exist in the dominant perovskite component. Using control volume based numerical models we investigate the impacts on mantle mixing of this spin transition through its influence on the most important subset of these physical properties, namely density, thermal expansivity, bulk modulus and heat capacity. Our numerical model results demonstrate that this electronic transition enhances mixing in the lower regions of the lower mantle by enhancing the vigor of rising plumes. The lowermost region of the mantle is slightly warmed and the upper mantle slightly cooled by spin-induced effects. However, the spin crossover in the lower mantle appears not to significantly influence mantle layering. Due to the competition that could exist between the strength of the spin-induced thermodynamic properties of ferropericlase and perovskite, cold descending thermal anomalies could stagnate at middle-to-lower mantle depths and lead to the occurrence of "mid mantle avalanches."

Citation: Shahnas, M. H., W. R. Peltier, Z. Wu, and R. Wentzcovitch (2011), The high-pressure electronic spin transition in iron: Potential impacts upon mantle mixing, *J. Geophys. Res.*, *116*, B08205, doi:10.1029/2010JB007965.

1. Introduction: The Spin Transition in Iron-Bearing Minerals Under Deep Mantle Conditions

[2] Our understanding of mantle dynamics relies strongly upon knowledge of the physical properties of mantle minerals. Two major constituent minerals of the lower mantle are aluminous silicate perovskite [Al–(Mg, Fe)SiO_3] and ferropericlase [(Mg, Fe)O] which volumetrically represent approximately 62% and 33% of the lower mantle respectively while the contribution of calcium silicate perovskite ($CaSiO_3$) represents only about 5% [*Ringwood*, 1982]. Numerical models of mantle convection are strongly dependent on our knowledge of the physical properties of mantle materials and any variation or change in these properties under deep mantle temperature and pressure conditions may fundamentally affect the style of convection, geochemical mixing and the rate of planetary cooling. Aside from the well known upper mantle phase transitions and the recently discovered deep mantle perovskite–post perovskite phase transition that occurs at about 2700 km depth [*Murakami et al.*, 2004; *Tsuchiya et al.*, 2004; *Oganov and Ono*, 2004], an "iron spin transition" in the lower mantle may also have significant impacts on mantle dynamics through its influence on mineral properties under lower mantle P-T conditions.

[3] The spin transition in iron from a high spin (HS) state as pressure (depth) increases to a low spin (LS) state was predicted five decades ago [*Fyfe*, 1960]. The occurrence of this spin transition in the mantle has also been predicted on the basis of both crystal field theory [*Burns*, 1993; *Sherman*, 1988] and band theory [*Cohen et al.*, 1997] to occur as a result of the compression of mantle material with increasing pressure. Until recently, however, there has been no direct experimental confirmation that the transition actually occurs.

[4] This transition is potentially important as it may result in changes of the fundamental physical properties of mantle minerals including radiative thermal conductivity, electrical conductivity, thermal expansivity, heat capacity, density, incompressibility, sound velocities and elastic moduli [*Lin et al.*, 2008; *Wentzcovitch et al.*, 2009; *Wu et al.*, 2009].

[1]Department of Physics, University of Toronto, Toronto, Ontario, Canada.
[2]Collaboratory for Advanced Computing and Simulations, University of Southern California, Los Angeles, California, USA.
[3]Minnesota Supercomputing Institute, University of Minnesota, Minneapolis, Minnesota, USA.

0148-0227/11/2010JB007965

Iron is a *3d* transition metal with two stable valence states, Fe^{2+} and Fe^{3+}, with electronic configurations [Ar] $3d^5$ and [Ar] $3d^6$, respectively. Although in crystalline environments the *3d* orbitals' degeneracy is lifted by the crystalline field, these orbitals remain fairly localized and can still be referred to their atomic counterparts. In cubic (octahedral) environments *3d* orbitals split into a lower energy triplet, the t_{2g} orbitals pointing away from the ligands, and into a higher energy doublet, the e_g orbitals pointing toward the ligands. The t_{2g}–e_g energy splitting is known as the crystal field splitting (CFS), denoted by Δ. As the pressure in the mantle increases with increasing depth the bond length between iron and oxygen in the mineral becomes shorter and the crystal field splitting parameter, which is inversely proportional to the Fe-O bond length, increases. Band dispersion of these orbitals also develops with decreasing bond lengths eventually leading to an insulator to metal transition, but this transition is not expected to take place at mantle pressures for ferropericlase or perovskite. Depending on the relative magnitude of Δ and of the electron paring energy (E_p), also known as Hunds rule energy, the lowest energy configuration of iron can either be high spin (HS), intermediate spin (IS), or low spin (LS), with total spin S = 2, 1, or 0 for Fe^{2+} respectively, or S = 5/2, 3/2, or 1/2 for Fe^{3+}. However, the increase in pressure doesn't essentially affect the pairing energy E_p and therefore the issue of whether the mineral is in an HS or an LS state is primarily determined by the magnitude of Δ. The crystal field splitting parameter Δ is low at low pressure (low density) and is high at high pressure (high density) corresponding to HS and LS states respectively [*Badro et al.*, 2005]. The HS-LS crossover decreases the number of unpaired *3d* electrons [*Burns*, 1993] and hence the magnetic susceptibility of the host phase decreases. The LS state of iron is expected to have a smaller ionic radius than its HS counterpart [*Shannon and Prewitt*, 1969]. These changes are expected to affect the thermoplastic properties of mantle materials [*Sherman*, 1988; *Wentzcovitch et al.*, 2009, *Lin et al.*, 2008] and consequently the style of mantle convection. The HS-LS crossover may also alter the chemical behavior of both ferropericlase and perovskite under high-pressure conditions thereby leading to a change in the iron content of these minerals through modification of the partition coefficient between ferropericlase and perovskite [*Badro et al.*, 2003]. This may have an important impact upon mantle dynamics because the content of iron in these mantle minerals affects their thermoelastic properties and melting points [e.g., *Badro et al.*, 2003].

[5] Some recent high-pressure experiments did reveal that a high-spin to low-spin (HS-LS) crossover in iron occurred in the range of pressure from 60 to 70 GPa in ferropericlase ($Mg_{0.83}Fe_{0.17}$) O [*Badro et al.*, 2003]. These early results based on high resolution Kβ X-ray spectroscopy (XES) revealed that the iron in ferropericlase is completely in the LS state at pressures greater than 75 GPa [*Badro et al.*, 2003]. The HS-LS crossover in ferropericlase had been earlier suggested on theoretical grounds to occur under just such mantle pressure conditions [e.g., *Sherman*, 1991]. However, on similar theoretical grounds the dominant perovskite component was first expected to remain in the HS state [*Cohen et al.*, 1997]. Arguments based on thermodynamics and crystal field theory have led to the notion that the HS-LS crossover in perovskite was inhibited throughout the Earth's mantle [*Hofmeister*, 2006]. However, some recent high-pressure experiments on perovskite suggested two possible electronic transitions to occur in iron at 70 GPa and 120 GPa corresponding to partial and maximum electron pairing in iron, respectively [*Badro et al.*, 2004].

[6] Although both theoretical and experimental work on ferropericlase confirm the HS-LS crossover in ferrous iron, the electronic transitions in perovskite are still debated [*Badro et al.*, 2003; *Lin and Tsuchiya*, 2008; *Lin et al.*, 2008; *Bengtson et al.*, 2009; *Hsu et al.*, 2010]. The most recent X-ray emission spectroscopy (XES) and synchrotron Mössbauer spectroscopy (SMS) data [*Lin et al.*, 2008] suggested that ferrous iron (Fe^{2+}) in perovskite and post perovskite remains in the intermediate-spin (IS) state in both phases. These authors concluded that changes in the radiative thermal conductivity and iron partitioning in the lowermost mantle would be controlled by the structural transition from perovskite to post perovskite, rather than by the electronic transition of Fe^{2+}. X-ray emission spectroscopy (XES) and nuclear forward scattering (NFS) data provide conflicting results and there are inconsistencies on the location, number and sharpness of the transition(s), and the valence states of iron are uncertain [*Badro et al.*, 2004; *Li et al.*, 2004, 2006; *Jackson et al.*, 2005; *McCammon et al.*, 2008]. The XES method cannot distinguish between the valence states of iron which contribute to the spin crossover transition. The total spin of iron versus pressure in perovskite, calculated using Mössbauer data [*McCammon et al.*, 2008] and taking into account contributions from the ferrous and ferric states, predicted a HS to IS transition in ferrous iron to occur under lower mantle conditions. Some recent results suggest different interpretations for the change in nuclear quadrupole splitting observed in the Mössbauer data which could be explained by a change in the orbital occupancy of the HS state due to a change in the position of ferrous iron in the perovskite cage rather than a change of spin state [*Bengtson et al.*, 2009; *Hsu et al.*, 2010]. However, the most recent experimental work of *Catalli et al.* [2010] reveals that all ferric iron in the B site makes the transition to a fully LS state at about 50–60 GPa. This transition increases both bulk modulus and density [*Catalli et al.*, 2009] below depths corresponding to this pressure range. If the high spin to low spin transition were to occur in both ferropericlase and perovskite the implications for mantle mixing would be extremely important as we will show in the analyses to be reported here.

2. Physical Properties Variations Due to the Spin Crossover Transition in Ferropericlase

[7] The pressure induced HS to LS transition in ferropericlase $Mg_{(1-x)}Fe_xO$ has both been observed in experiments [*Badro et al.*, 2003] and predicted on the basis of theoretical calculation [*Tsuchiya et al.*, 2006]. This phenomenon has been extensively investigated in the past decade [*Badro et al.*, 2003; *Crowhurst et al.*, 2008; *Goncharov et al.*, 2006; *Lin et al.*, 2005, 2007, 2008; *Fei et al.*, 2007; *Speziale et al.*, 2005; *Sturhahn et al.*, 2005; *Tsuchiya et al.*, 2006; *Wu et al.*, 2009]. The spin transition is sharp at low temperature but broadens with increasing temperature [*Sturhahn et al.*, 2005; *Tsuchiya et al.*, 2006; *Lin et al.*, 2007; *Wentzcovitch et al.*, 2009; *Wu et al.*, 2009]. At 2000 K, it occurs between 53 GPa (for $n = 0.1$) and 86 GPa (for $n = 0.9$)

[*Wentzcovitch et al.*, 2009; *Wu et al.*, 2009], where n is the fraction of the LS state. The spin crossover is a continuous phenomenon passing through a mixed spin (MS) state, consisting of HS and LS irons coexisting simultaneously. Throughout the MS state thermodynamic properties are significantly modified [*Wentzcovitch et al.*, 2009; *Wu et al.*, 2009], including a possible change in viscosity [*Wentzcovitch et al.*, 2009]. The predicted softening of the bulk modulus has actually been observed experimentally [*Crowhurst et al.*, 2008].

[8] To understand the origin of the "anomalies" in the thermodynamic properties throughout the MS state it is useful to refer to the thermodynamic formalism of this uncommon solid solution. Ferropericlase in the MS state is described as an ideal solid solution (ISS) of pure HS and LS ferropericlase [*Wentzcovitch et al.*, 2009; *Wu et al.*, 2009]. The Gibbs free energy of the MS state, $G(n, P, T)$, is then given by

$$G(n,P,T) = nG_{LS}(P,T) + (1-n)G_{HS}(P,T) + k_B T X_{Fe} [n\ln(n) + (1-n)\ln(1-n)] \quad (1)$$

where $n \equiv n(P, T)$ is the fraction of LS states in the mixture, G_{LS} and G_{HS} are respectively the Gibbs free energies of the pure LS and HS states, and the last term is the free energy of mixing of the ideal HS-LS mixture. The Gibbs free energy of the pure (HS or LS) states is

$$G_{HS/LS}(P,T) = G^{stat+vib}_{HS/LS}(P,T) + G^{mag}_{HS/LS} \quad (2)$$

where $G^{stat+vib}_{HS/LS}(P, T)$ is the Gibbs free energy containing static and vibrational contributions in either the HS or the LS state, and $G^{mag}_{HS/LS}$ is the magnetic contribution:

$$G^{mag}_{LS} = 0 \quad (3a)$$

$$G^{mag}_{HS} = -k_B T X_{Fe} \ln[m(2S+1)] \quad (3b)$$

where $S = 2$ and $m = 3$ are respectively the spin and electronic configuration (orbital) degeneracy of iron in the HS state. Minimizing the free energy in equation (1) with respect to the LS fraction, n, leads to

$$n(P,T) = \frac{1}{1 + m(2S+1)\exp\left[\frac{\Delta G^{stat+vib}_{LS-HS}}{X_{Fe}k_B T}\right]} \quad (4a)$$

where

$$\Delta G^{stat+vib}_{LS-HS} = G^{stat+vib}_{LS}(P,T) - G^{stat+vib}_{HS}(P,T) \quad (4b)$$

and where $G^{stat+vib}_{LS}$ and $G^{stat+vib}_{HS}$ are the Gibbs free energies containing static and vibrational contributions at low and high spin states respectively [*Wentzcovitch et al.*, 2009; *Wu et al.*, 2009]. Since at equilibrium $\frac{\partial G(n)}{\partial n}|_{T,P} = 0$, one gets

$$V(n) = nV_{LS}(P,T) + (1-n)V_{HS}(P,T) \quad (5)$$

The thermal expansion coefficient of the MS state is by definition

$$\alpha(n) = \frac{1}{V(n)}\left(\frac{\partial V(n)}{\partial T}\right)_P \quad (6)$$

Thus we have

$$\alpha(n)V(n) = nV_{LS}\alpha_{LS} + (1-n)V_{HS}\alpha_{HS} + (V_{LS} - V_{HS})\left.\frac{\partial n}{\partial T}\right|_P \quad (7)$$

Similarly, for the isothermal bulk modulus of the MS state, which is defined as

$$K_T(n) = -V(n)\left(\frac{\partial P}{\partial V(n)}\right)\Big|_T \quad (8)$$

Evaluation of this quantity delivers the result

$$\frac{V(n)}{K_T(n)} = n\frac{V_{LS}}{K_{T_{LS}}} + (1-n)\frac{V_{HS}}{K_{T_{HS}}} - (V_{LS} - V_{HS})\left.\frac{\partial n}{\partial P}\right|_T \quad (9)$$

[9] In the spin crossover region, where n depends on the pressure and temperature, the last terms in equations (7) and (9) contribute considerably to the thermodynamic properties of the ferropericlase in the MS state. Noting that the LS state has a smaller volume than that of the HS state and that n decreases with temperature and increases with pressure, the spin crossover will always increase the thermal expansivity and decrease the bulk modulus in the crossover regime.

[10] The anomalies in thermodynamic properties in the MS regime are determined by the difference in thermodynamic properties between the mixed spin (MS) state and the HS state. The temperature and pressure dependences of spin-induced anomalies of density, thermal expansivity, bulk modulus and heat capacity are illustrated in Figure 1. The density of the MS state is a weighted average of the density of the HS and LS states. The anomaly in density increases with pressure monotonically since the fraction of the LS state increases with pressure and the LS state has higher density than the HS state. The HS and LS states have similar thermal expansivity and heat capacity. Therefore, the anomalies in the thermal expansivity and heat capacity are negligible outside of the crossover region. Nevertheless, they become highly significant inside the crossover region. For example, the anomaly in thermal expansivity (15×10^{-5}/K) is about ten times larger than the thermal expansivity of the HS state (1.5×10^{-5}/K) at 300 K and 40 GPa. At 2000 K and 70 GPa, the anomaly is still about 50% larger than the thermal expansion coefficient characteristic of the HS state. The significant anomalies in thermodynamic properties such as thermal expansivity result from the sensitivity of the fraction of the LS state to temperature and pressure within the spin crossover region. Decreasing (increasing) the fraction of the LS state can cause the volume of the MS state to expand (contract) since the HS state has larger volume than the LS state. This additional volume change is the fundamental reason for the anomalies in thermal expansivity and the bulk modulus, which is clearly evident in the formulae describing the thermal expansivity and bulk modulus of the MS state which are discussed in what follows.

3. Numerical Formulation of the Problem of Mantle Convection in the Presence of the Iron Spin Transition

[11] The set of thermomechanical equations at high Prandtl number (effectively infinite) for an anelastically compressible

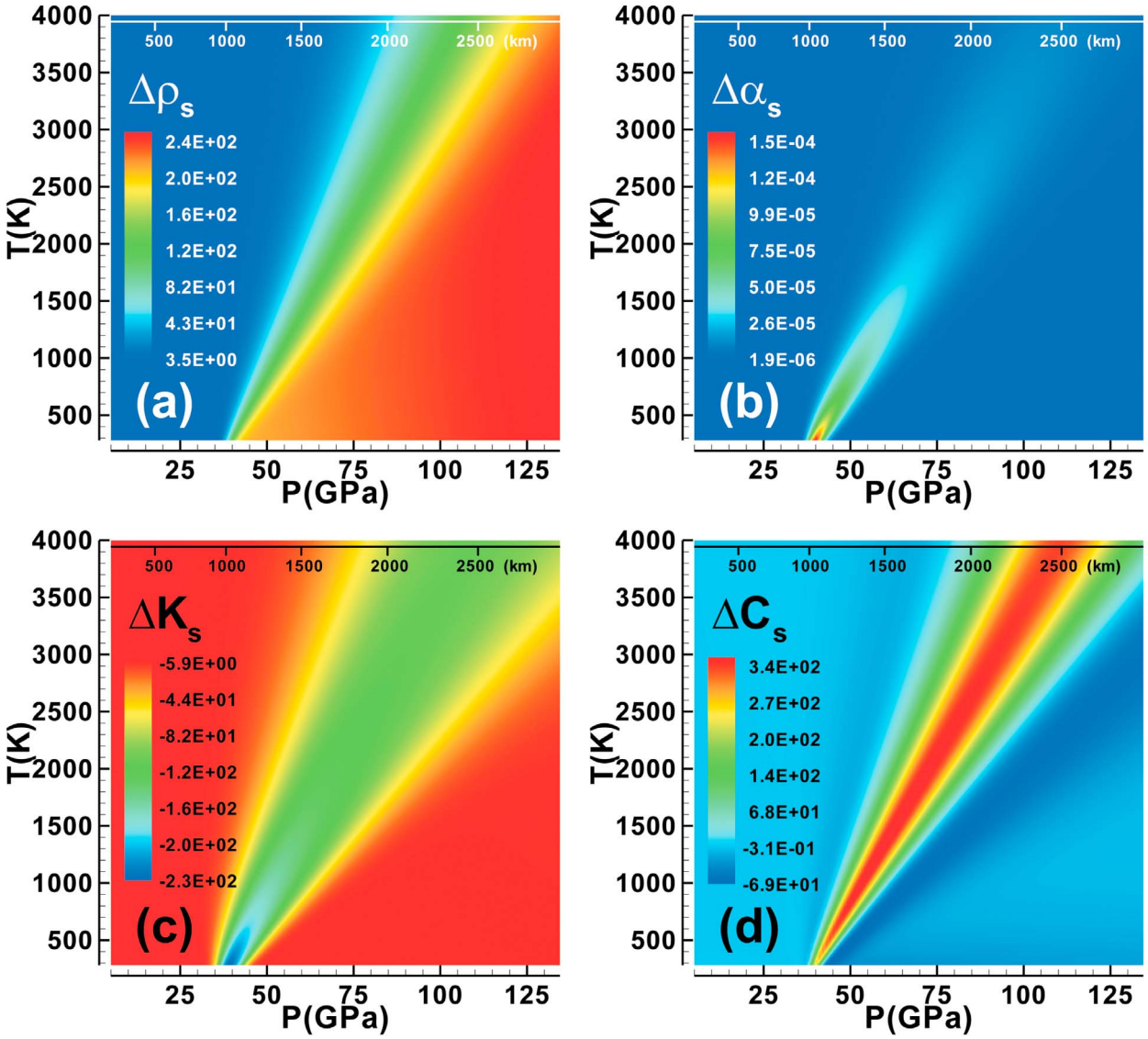

Figure 1. Pressure and temperature dependence of spin-induced anomalies in (a) density in kg/m^3, (b) thermal expansivity in 1/K, (c) bulk modulus in GPa, and (d) heat capacity in J/kg/K in ferropericlase ($Mg_{(1-x)}Fe_xO$) with X = 0.1785. The anomalies are determined by the difference in thermodynamic properties between the mixed spin (MS) state and the HS state [*Wu et al.*, 2009]. The scale represents the depth in the mantle.

fluid consist of the flowing conservation laws, respectively for mass, momentum and internal energy [*Peltier et al.*, 1997; *Solheim and Peltier*, 1993, 1994a, 1994b]:

$$\nabla \cdot \left(\overline{\rho}\vec{V}\right) = 0 \tag{10}$$

$$-\nabla P + \nabla \cdot \overline{\overline{\sigma}} - \rho g\hat{r} = 0 \tag{11}$$

$$C_P\overline{\rho}\frac{DT}{Dt} - \alpha T\frac{DP}{Dt} = \nabla \cdot (k\nabla T) + \Phi + \overline{\rho}H + \overline{\rho}l_i\frac{D\Gamma_i}{Dt} \tag{12}$$

in which $\overline{\rho}$ is the depth dependent and time-independent background density that characterizes the anelastic reference state upon which thermally forced convection described by the above equations is superimposed. Numerical solutions to this set of field equations are constructed using a compressible control volume methodology [*Patankar and Spalding*, 1972; *Patankar*, 1980; *Shahnas and Peltier*, 2010]. The deviatoric stress tensor that appears in the quasi-static momentum balance equation (11) is given by

$$\overline{\overline{\sigma}} = \eta\left[\nabla\vec{V} + \left(\nabla\vec{V}\right)^T\right] - \frac{2}{3}\eta\left(\nabla \cdot \vec{V}\right)\bar{I} \tag{13}$$

[12] The equation of state for density that is required to close the field theory in the absence of influence of the spin transition will be assumed to include the influence of the Olivine–Spinel, Spinel–Pv + Magnesiowustite and Pv–pPv phase transitions at 410 km, 660 km and 2700 km depths

respectively. This spin transition free version of the equation of state is represented as

$$\rho = \overline{\rho}\left[1 - \alpha(T - T_r) + \frac{1}{K_T}(p - p_r)\right] + \Delta\rho_i(\Gamma_i - \Gamma_{ri}) \quad i = 1, 2, 3 \tag{14}$$

[13] In the above closed system of equations the variables ρ, g, α, T, V, p, η, C_P, k, K_T, and t respectively denote density, gravitational acceleration, thermal expansivity, temperature, velocity, pressure, dynamic viscosity in shear, heat capacity at constant pressure, thermal conductivity, bulk modulus at constant temperature, and time. $\Delta\rho_i$ is the density contrast between two solid phases across phase transition i and Γ_i is a phase density functional defined by

$$\Gamma_i = \frac{1}{2}[1 + \tanh(\pi_i)] \qquad i = 1, 3 \tag{15}$$

in which the nondimensional arguments of the hyperbolic tangent functions are given by

$$\pi_i = \frac{d_i - d - \gamma_i(T - T_i)}{h_i} \tag{16}$$

in which d, d_i, h_i, T_i, and γ_i are depth, reference depth of phase boundary i, width of the ith divariant phase transition i, transition temperature at the reference depth d_i and the Clapeyron slope of the relevant phase transition, respectively. The quantity Φ represents the viscous dissipation rate per unit volume in the mantle flow, and has the following explicit form [*Solheim and Peltier*, 1993] in the case of axisymmetric spherical flow upon which we will focus for present purposes:

$$\Phi = \eta\left\{2\left[\frac{\partial V_r}{\partial r}\right]^2 + 2\left[\frac{1}{r}\frac{\partial V_\theta}{\partial\theta} + \frac{V_r}{r}\right]^2 + 2\left[\frac{V_r}{r} + \frac{V_\theta \mathrm{Cot}(\theta)}{r}\right]^2\right\} + \eta\left\{\left[\frac{\partial V_\theta}{\partial r} - \frac{V_\theta}{r} + \frac{1}{r}\frac{\partial V_r}{\partial\theta}\right]^2 - \frac{2}{3}\left[\nabla\cdot\vec{V}\right]^2\right\} \tag{17}$$

[14] Insofar as the functional form to be employed for the pressure and temperature-dependent thermal conductivity is concerned, we will employ the semiempirical representation proposed by *Hofmeister* [1999], as

$$k(P,T) = k(298)\left(\frac{298}{T}\right)^a \exp\left[-\left(4\gamma + \frac{1}{3}\right)\int_{298}^{T}\alpha(\theta)d\theta\right]\left(1 + \frac{K_o'}{K_o}\right) + \sum_0^3 b_i T^i \tag{18}$$

The first and second terms in this equation describe the lattice vibration (phonon) and radiative transport (photon) contributions to the thermal conductivity respectively. The thermal conductivity has been restricted to have a lowest value of 2.5 $\mathrm{Wm^{-1}\,K^{-1}}$ near the surface. In the present work the pressure and temperature dependent thermal expansivity will be calculated from [e.g., *Fei*, 1995; *Schmeling et al.*, 2003]

$$\alpha(p,T) = \alpha_o(T)\left(\frac{V(p,T)}{V(0,T)}\right)^{\delta_T} \tag{19}$$

in which $V(p, T)/V(0, T)$ can be obtained from the third order Birch-Murnaghan equation of state as

$$p = 3f(1 + 2f)^{5/2}K_{T_o}(T)\left[1 - \frac{3}{2}(4 - K_0')f\right] \tag{20}$$

In this equation f is the compression defined by

$$f = \frac{1}{2}\left[\left(\frac{V(0,T)}{V(p,T)}\right)^{2/3} - 1\right] \tag{21}$$

and δ_T in equation (19) is the Anderson-Gruneisen parameter, V represents the volume at pressure p and temperature T; $K_{T_o}(T)$ and K_o' are the bulk modulus and its pressure derivative respectively. For the temperature dependent part of this coefficient, a power law relation which fits the experimental data over a specific temperature range [*Fei*, 1995] has been employed as

$$\alpha_o(T) = a_o + a_1 T + a_2 T^{-2} \tag{22}$$

[15] For temperatures higher than the Debye temperature, δ_T and αK_T are almost independent of temperature and the bulk modulus may be written as [*Kumar*, 2000]:

$$K_{To}(T) = K_o\left[1 - \alpha_o\delta_T^o(T - T_o)\right] \tag{23}$$

The model parameters for both thermal conductivity and thermal expansivity are presented in Tables 1a and 1b.

4. Mantle Convection in the Presence of the Iron Spin Transition: Results

[16] In order to describe the impact upon the convection process of the iron spin crossover in the lower mantle through its impacts on density, thermal expansivity, bulk modulus and heat capacity, we have employed axisymmetric control volume based spherical models of this dynamical system [*Patankar*, 1980; *Shahnas and Peltier*, 2010] in the limit of infinite Prandtl number as is appropriate for Earth's mantle in which the kinematic viscosity is extremely high relative to the thermal diffusivity. In the models to be discussed in what follows we have employed a radial viscosity profile based directly upon the results obtained through the analysis of isostatic adjustment observations, namely the VM3 viscosity model of *Peltier* [1998]. In the work of *Peltier and Drummond* [2010], this model has been shown to satisfy the detailed constraints upon the viscosity of the lower mantle provided by observed Earth rotation anomalies related to the Late Quaternary ice age cycle. A present-day internal heating rate of 13 TW which is uniformly distributed throughout the mantle will be assumed for the purpose of all model analyses, a level of internal heating that is close to the requirement of Chondritic meteorites (see *Butler and Peltier* [2002] for discussion). The models have isothermal cores with a core-mantle boundary temperature of either 3600 K or 4000 K and a temperature at Earth's surface of 293 K with free slip boundary conditions imposed on both top and bottom boundaries. The models do not therefore explicitly account for the influence of the surface plates. As previously discussed, analyses will be based upon models that also include the traditional phase transitions that occur

Table 1a. The Parameters for Pressure And Temperature-Dependent Thermal Conductivity Used in Equation (18)[a]

Parameter	Value
$k(298)$	4.7 Wm^{-1} K^{-1}
a	0.3
γ	1.2 K
K_o'	4
K_o	261 GPa
b_o	1.7530×10^{-2}
b_1	-1.0365×10^{-4}
b_2	2.2451×10^{-7}
b_3	-3.4071×10^{-11}

[a]*Hofmeister* [1999] and *van den Berg et al.* [2002].

at 410 km and 660 km depth which bracket the mantle transition zone that separates the upper mantle above 410 km from the lower mantle below a depth of 660 km. In several models we have also included the recently discovered perovskite–post perovskite deep mantle phase transition which occurs at approximately 2700 km depth and which appears to define the top of the D'' layer. All numerical models will assume effective Clapeyron slopes of 3.0 MPa/K and −3.0 MPa/K, together with density contrasts of 200 kg/m^3 and 440 kg/m^3 at the exothermic and endothermic phase transition boundaries at 410 km and 660 km depths respectively. The impact of the iron spin transition will be compared and discussed for models which either include or exclude the Pv–pPv deep mantle phase transition.

[17] In order to analyze the impact of anomalies in physical properties arising from the presence of the iron spin transition in the lower mantle we will first consider the impact of the spin transition induced anomaly in each property separately. In these models the equation of state (14) is sequentially replaced by the following forms which respectively include the influence of the density anomaly $\Delta\rho_s$, the thermal expansivity anomaly $\Delta\alpha_s$, and the bulk modulus anomaly ΔK_s:

$$\rho_{\rho}^{spin} = \overline{\rho}\left[1 - \alpha(T - T_r) + \frac{1}{K_T}(p - p_r)\right] + \Delta\rho_i(\Gamma_i - \Gamma_{ri}) + \Delta\rho_s \tag{24}$$

$$\rho_{\alpha}^{spin} = \overline{\rho}\left[1 - [\alpha + \Delta\alpha_s](T - T_r) + \frac{1}{K_T}(p - p_r)\right] + \Delta\rho_i(\Gamma_i - \Gamma_{ri}) \tag{25}$$

$$\rho_{K}^{spin} = \overline{\rho}\left[1 - \alpha(T - T_r) + \frac{1}{K_T + \Delta K_s}(p - p_r)\right] + \Delta\rho_i(\Gamma_i - \Gamma_{ri}) \tag{26}$$

The net effect of the iron spin transition on density is described by the superposition of these effects and is represented by

$$\rho_{\rho\alpha K}^{spin} = \overline{\rho}\left[1 - [\alpha + \Delta\alpha_s](T - T_r) + \frac{1}{K_T + \Delta K_s}(p - p_r)\right] + \Delta\rho_i(\Gamma_i - \Gamma_{ri}) + \Delta\rho_s \tag{27}$$

In several of the models to be discussed in what follows we have also considered only the combined effect of the spin-induced density anomaly and the spin-induced expansivity anomaly in the state equation as

$$\rho_{\rho\alpha}^{spin} = \overline{\rho}\left[1 - [\alpha + \Delta\alpha_s](T - T_r) + \frac{1}{K_T}(p - p_r)\right] + \Delta\rho_i(\Gamma_i - \Gamma_{ri}) + \Delta\rho_s \tag{28}$$

[18] The spin transition in the lower mantle also impacts the heat capacity and hence the convection process; however, this impact is not significant. The total heat capacity is the superposition of the reference heat capacity and the contribution arising from the spin transition ΔC_s, namely:

$$C_P^{spin} = C_P + \Delta C_s \tag{29}$$

where the constant term is taken to be 1250 J/kg/K. All these spin-induced anomalies ($\Delta\rho_s$, $\Delta\alpha_s$, ΔK_s and ΔC_s) in the MS regime are determined by the difference in relevant properties between the mixed spin (MS) state and the HS state at a given pressure and temperature. The spin-induced density, thermal expansivity, bulk modulus anomalies employed in equations (24)–(26) and the heat capacity anomaly are graphically represented in Figure 1 which have been obtained by subtracting the relevant set of data in the case in which no HS-LS transition occurs (purely HS state) from the set of data in which the HS-LS spin transition is assumed to exist [*Wu et al.*, 2009].

[19] The model nomenclature to be employed in the discussion of the results is such that each model designation begins with the letter "C" representing the Clapeyron slope of the Pv–pPv transition which is followed by two digits specifying the magnitude of the assumed Clapeyron slope in MPa/K. This initial designation is followed by the letter "D" and two digits specifying the density contrast across this transition in kg/m^3. Since all models described here include both exothermic and endothermic phase transitions at 410 km and 660 km depths, for example the model *C*00*D*00 include only the solid-solid phase transitions at 410 km depth and 660 km depth and the model *C*08*D*80 further to these phase transitions include the deep mantle Pv–pPv transition with the Clapeyron slope and density contrast of 8 MPa/K and 80 kg/m$_3$ respectively. Finally the model name is terminated with either *Ref*, ρ, α, *K*, or C_P, specifying the reference model (equation (14)), the model with density anomaly (equation (24)), the thermal expansivity anomaly (equation (25)), the bulk modulus anomaly (equation (26)), or the heat capacity anomaly respectively (equation (29)). There are also models which include the

Table 1b. The Parameters for Pressure and Temperature-Dependent Thermal Expansivity Used in Equations (19)–(23)[a]

Parameter	Value
a_o	3.034×10^{-5} K^{-1}
a_1	7.422×10^{-9} K^{-2}
a_2	−0.5381 K
K_o	129 GPa
α_o	2.64×10^{-5} K^{-1}
δ_T^o	5.5
T_o	298 K
K_o'	5.37

[a]*Fei* [1995] and *Schmeling et al.* [2003].

combined effect of all these anomalies which will be specified by including the appropriate combination of these anomalous property symbols.

[20] Before presenting the numerical model results it will be instructive to consider the influence of spin-induced anomalies in the lower mantle separately. To clarify this point we illustrate the depth dependence of all spin-dependent anomalies for a cold (1200 K) and hot (2500 K) temperature as well as for a sample geotherm for a model with all three solid-solid phase transitions included (*C*08*D*80) and VM3 radial viscosity profile in Figure 2, where $\Delta\rho_s$ has already been described and the variations of $\Delta\rho_\alpha$ and $\Delta\rho_K$ shown in the individual panels are given by

$$\Delta\rho_\alpha = -\overline{\rho}\Delta\alpha_s(T - T_r) \tag{30}$$

$$\Delta\rho_K = \overline{\rho}\left[\left(\frac{1}{K_T + \Delta K_s} - \frac{1}{K_T}\right)(p - p_r)\right] \tag{31}$$

4.1. Iron Spin Crossover in Ferropericlase

[21] Focusing first upon the case in which the spin transition is assumed to occur only in the ferropericlase component of the mineralogy, inspection of Figure 2c shows that the spin-induced density anomaly monotonically increases with depth as the transition from the HS state to the LS state occurs until the mantle mineral(s) have fully executed the transition to the LS state (except for the very hot CMB region as will be clear by inspection of Figure 2c). However, the spin-induced anomalies in thermal expansivity and bulk modulus induce negative and positive density anomalies respectively which first increase and then decease in magnitude (except in the very hot CMB region displayed in Figure 2c) as the HS-LS transition takes place. Based upon Figure 2a the overall effect of spin induced density anomalies (the solid line) is such that as a result of the positive density anomaly gained by the overall effect of the spin-induced density, thermal expansivity and bulk modulus anomalies, a cold descending slab (1200 K) is first accelerated (in the depth range from ~900–1600 km) and then is decelerated due to the density reduction. Below ~2000 km depth the cold slab is once again slightly accelerated. Similarly, a hot rising plume (2500 K), as can be conjectured from the overall effect of the spin-induced density anomalies shown by the solid line in Figure 2b is first accelerated (below ~1900 km depth) and then decelerated (in the same depth range from ~1900–1600 km) due to first a reduction and then an increase in overall density anomaly respectively as the plume continues to rise. The rising plume again experiences acceleration between ~1600 km depth and ~900 km depth (Figure 2b).

[22] Figures 2a and 2b reveal that the overall effect of the above mentioned spin-induced anomalies (the solid lines) is such that the vigor of convection is increased by either cold descending anomalies or by hot rising plumes below ~1900 km depth. The density anomalies due to the spin-induced thermal expansivity anomaly and the spin-induced bulk modulus anomalies are competing with each other (the anomalies are opposite in sign) and hence the estimates of the strength of these anomalies are crucial in determining the consequences of the spin transition effect. As an extreme end-member example we also consider a model in which only the effect of the spin-induced density anomaly and spin-induced thermal expansivity anomaly are present, again assuming that transition occurs only in the ferropericlase component of the mineralogy. Figure 2 reveals that, in the models that include $\Delta\rho_s + \Delta\rho_\alpha$ the rising hot plumes (see dashed double-dotted line in Figure 2b) first accelerate and then decelerate (as the LS-HS spin transition takes place). On the other hand anomalously cold descending material (see dashed double-dotted line in Figure 2a) first decelerates and then accelerates (as the HS-LS spin transition takes place). In the latter case, however, flow stagnation in the mid mantle region may occur. We will return to this issue at the end of this section where we will present our final model of this kind.

[23] In the first sequence of the numerical results under discussion here we assume that there is no spin crossover and hence no anomaly in material properties in the perovskite component of mantle mineralogy and investigate the impacts of the spin crossover in the case in which it exists in ferropericlase only, a component of lower mantle mineralogy that constitutes approximately 33% volumetrically of the constituent minerals. In this sequence of numerical models we have taken this fact into account by reducing the magnitude of the anomalies by a factor of 3 (1/3 of the amplitude of anomalies shown in Figures 1 and 2). The models that include the Pv–pPv phase transition in this sequence characterize this phase transformation by a Clapeyron slope and density contrast of 8 MPa/K and 80 kg/m^3 respectively. This sequence of models includes two subsequences which differ from each other in their CMB temperatures which have been fixed either at 3600 K [*Boehler*, 1992], or at 4000 K as previously mentioned. All models were run until a statistically steady state was achieved such that no long-term trends in mean temperature, surface heat flow or kinetic energy were observed. The time averaged geotherms and absolute radial mass flux profile [*Peltier and Solheim*, 1992], for these models are displayed in Figure 3 for the two CMB temperatures and are compared with the reference models which do not include the spin transition effect. The mantle geotherms in Figures 3a and 3c demonstrate that in the models with spin-induced anomalies the upper mantle is slightly cooler than those in their reference model counterparts (with no spin-induced effects). In contrast in the deep mantle region the mean mantle temperature in the models that include spin transition effects is slightly higher. Also the region just below the endothermic transition zone in general is slightly cooler in these models and the mantle adiabats have slightly shifted toward the superadiabatic. Compared to the reference models the mixing is still strong in the lower mantle (Figures 3b and 3d) but in this case there is no significant impact upon the degree of mantle layering.

4.2. Contribution to the Bulk Modulus Anomaly From the Spin Transition in Perovskite

[24] Although some recent experimental results suggest that perovskite remains in the intermediate spin state at pressures and temperatures consistent with deep mantle conditions, and therefore that the changes in the properties of the perovskite phase are likely to be dominated by the structural phase transition of Pv to pPv rather than the electronic transition of Fe^{2+} [*Lin et al.*, 2008; *McCammon et al.*, 2008], the spin state of ferric iron under deep mantle conditions remains unclear [*Zhang and Oganov*, 2006]. Some of the most recent

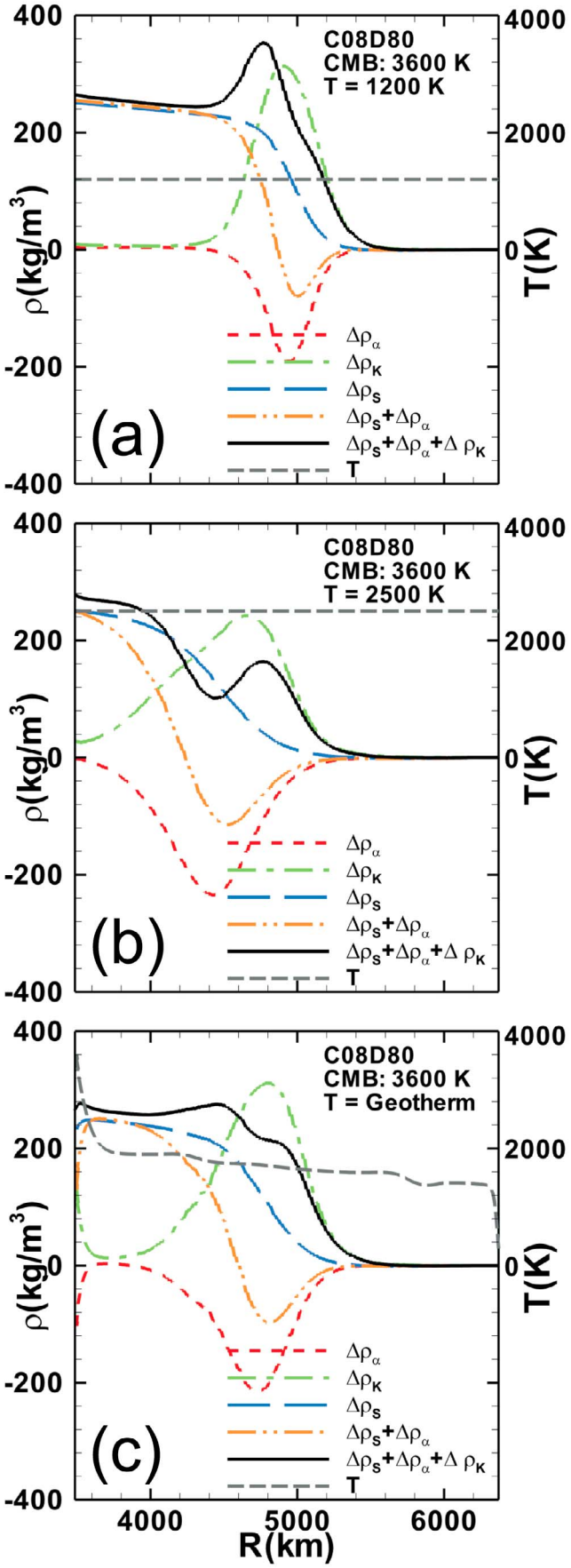

experimental work reveals that although a spin transition in ferrous iron likely has no effect on the density or bulk modulus of perovskite [*Lundin et al.*, 2008]; however, all ferric iron in the B site gradually makes a transition to a fully LS state at about 50–60 GPa [*Catalli et al.*, 2010] causing anomalies both in density [*Catalli et al.*, 2009] and bulk modulus [*Catalli et al.*, 2010]. Based on these experimental results there should exist an approximately 14% further increase in bulk modulus associated with the spin transition of Fe^{3+}. Figure 4 displays the overall spin-induced anomaly in bulk modulus which is a weighted superposition of the individual anomalies in ferropericlase and perovskite with the weighting factors of 1/3 and 2/3 based on the volumetric contribution of these minerals to the lower mantle mineralogy, respectively. The data employed in this superposition in the case of ferropericlase is based on the data graphically presented in Figure 1c. In the case of perovskite we have assumed a 14% increase in bulk modulus which occurs in the range of 50–60 GPa [*Catalli et al.*, 2010]. The influence of this increase in bulk modulus (see equations (26) and (31)) is such that, below the depth at which this transition occurs, uprising mantle plumes become less buoyant and the descending cold anomalies become more buoyant. This fact is demonstrated in Figure 5 (the solid lines) in which we have assumed a spin transition in the valence of Fe^{2+} in ferropericlase (inducing anomalies in the density, thermal expansivity and bulk modulus) and in the valence of Fe^{3+} in perovskite (inducing an anomaly in the bulk modulus) weighted by 1/3 and 2/3 respectively. Unlike the case displayed in Figure 2 for pure ferropericlase the overall effect of spin-induced anomalies which includes the contribution from bulk modulus anomaly in perovskite is such that the total density anomaly (solid line) for a cold descending slab (1500 K) becomes negative at about 1500 km depth. The slab is first accelerated above ~1300 km depth and then is strongly decelerated below this depth and above ~1500 km depth where the slab may stagnate at this midmantle horizon. Similarly a hot rising plume (2500 K) below a depth of about 1500 km is first accelerated but then strongly decelerated. Similar to the cold descending temperature anomalies the hot rising plumes may also stagnate at this midmantle horizon. Although there is as yet no reliable data available concerning the magnitude of the density anomaly associated with the spin transition in the perovskite component of the mineralogy, the most recent studies reveal that Fe^{3+}–Al-bearing perovskite is denser in the lowermost mantle than previously thought due to the Fe^{3+} spin transition and Fe^{3+}–Al site mixing [*Catalli et al.*, 2010]. Insofar as the thermal expansivity anomaly in the perovskite phase is concerned, there is at present no reliable data available. We are therefore not in a position as yet to perform analyses of its additional impact upon the mixing process as we have been able to do for ferropericlase. In section 4.4 we

Figure 2. Depth (pressure) dependence of the density anomalies $\Delta\rho_s$, $\Delta\rho_\alpha$, and $\Delta\rho_K$ and the superposition of these anomaly components $\Delta\rho_s + \Delta\rho_\alpha$ and $\Delta\rho_s + \Delta\rho_\alpha + \Delta\rho_K$ in the models *C08D80* due to the spin crossover in ferropericlase in the lower mantle as discussed in the section 4.1 for (a) a low temperature at 1200 K, (b) a high temperature at 2500 K, and (c) a sample mantle geotherm.

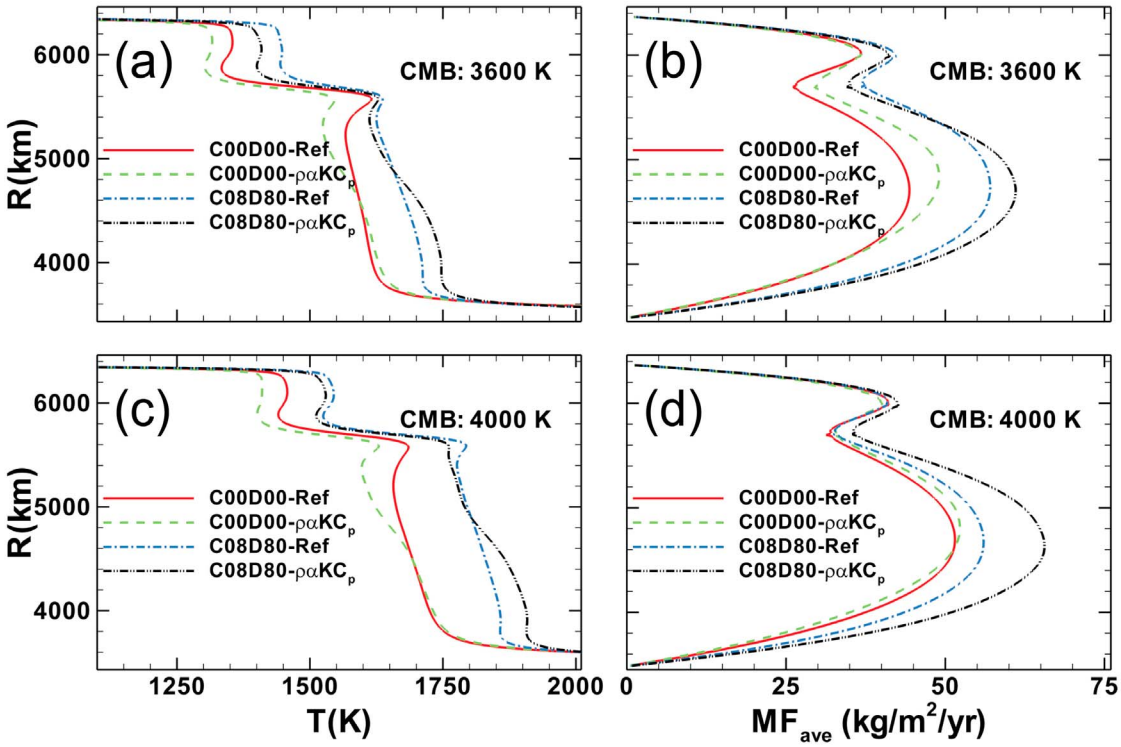

Figure 3. (a) Geotherms for the models with and without Pv–pPv phase transition in the presence of lower mantle spin crossover in ferropericlase ($C00D00 - \rho\alpha KC_P$ and $C08D80 - \rho\alpha KC_P$) are compared with the reference model counterparts ($C00D00 - Ref$ and $C08D80 - Ref$) with no spin crossover effects (i.e., the models fully in the HS state consistent with PREM mantle density profile) assuming a 3600 K CMB temperature. (b) Time-averaged absolute radial mass flux profiles for the models described in Figure 3a. (c) Similar to Figure 3a but with CMB at 4000 K. (d) Similar to Figure 3b but with CMB at 4000 K.

will nevertheless speculate on its possible contribution in the context of the analysis of an end-member model.

4.3. Iron Spin Crossover in Both Ferropericlase and Perovskite

[25] In the second sequence of numerical models our goal is to explore the importance of the strength as well as the relative importance of spin-induced anomalies and their impacts on mantle dynamics. To accomplish this we assume the occurrence of strong spin-induced anomalies as would be expected in the case in which all of the spin-induced property changes also occur in the perovskite phase. Based upon this assumption the strength of spin-induced anomalies are similar to those displayed in Figure 2 (superposition of the volumetric fractions 1/3 and 2/3 of the quantities shown in Figure 1 for ferropericlase and perovskite respectively). The time averaged geotherms and absolute radial mass flux profiles [*Peltier and Solheim*, 1992], for these models are displayed in Figure 6 for the models with CMB temperature of 4000 K (similar results were obtained for the models with CMB temperature of 3600 K but are not shown). A singular feature is observed to characterize the results for all models that include only the thermal expansivity anomaly or only the bulk modulus anomaly. There is a large reduction in CMB heat flux in the models that include only the thermal expansivity anomaly or only the bulk modulus anomaly and hence a very low surface heat flux as well.

[26] Inspection of the geotherms in Figure 6 shows that compared to the reference models ($C00D00 - Ref$, $C08D80 - Ref$) the influence of the spin-induced thermal expansivity acting alone ($C00D00 - \alpha$, $C08D80 - \alpha$) and that of the spin-induced bulk modulus acting alone ($C00D00 - K$, $C08D80 - K$) have increased the lower mantle temperature below about 1400 km depth and 1900 km depth respectively. However, above these depths the mantle is cooler than the thermal regime characteristic of the reference models in the absence of spin transition influence. In the models with only the thermal expansivity anomaly or only the bulk modulus anomaly, depending on the thermal state of the planet (core temperature and/or Pv–pPv phase transition parameters), the mantle may exhibit episodic but catastrophically rapid convective overturns in which the mean mantle temperature may increase by a few hundred degrees within a few tens of millions of years. This feature is illustrated in Figures 7 and 8 for the models $C08D80 - \alpha$ and $C08D80 - K$ with the CMB temperature of 4000 K (similar features were observed in the models with CMB temperature of 3600 K but are not shown). The mean mantle temperature, geotherm and time-averaged radial mass flux for these two models are shown in Figure 7. The temperature field snapshots for

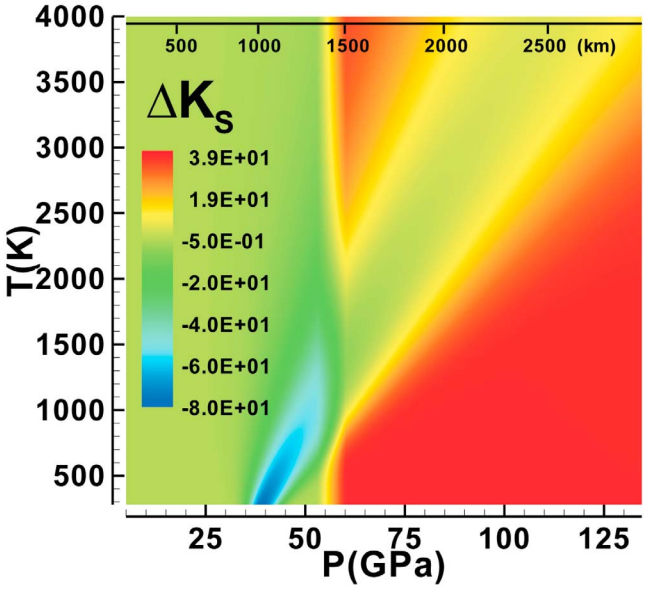

Figure 4. Pressure and temperature dependence of total spin-induced bulk modulus anomaly (in GPa) in ferropericlase and perovskite mixture [*Wu et al.*, 2009; *Catalli et al.*, 2010]. The contributions arising from ferropericlase and perovskite are weighted by a factor of 1/3 and 2/3 respectively in this superposition. The scale represents the depth in the mantle.

these models at the times indicated (t_1–t_5 for the model $C08D80 - \alpha$ and t_1'–t_5' for the model $C08D80 - K$) are illustrated in Figure 8. In Figure 8 the snapshots shown at t_1 and t_1' represent the statistically steady states just prior to the occurrence of the rapid convective overturn. As can be seen from Figures 7a and 7d, a sudden increase in mean mantle temperatures within a short period of time are about 300 K and 120 K in models $C08D80 - \alpha$ and $C08D80 - K$ respectively. Figures 7b and 7e illustrate the evolution of the mantle geotherms corresponding to the evolution times shown in Figures 7a and 7d (see also Figure 8). Following this rapid mantle mixing event it takes billions of years before a geotherm similar to the snapshots shown at t_1 or t_1' (Figures 7b and 7e) approaches to a similar form and another such mixing event is triggered. Figures 7c and 7f compare

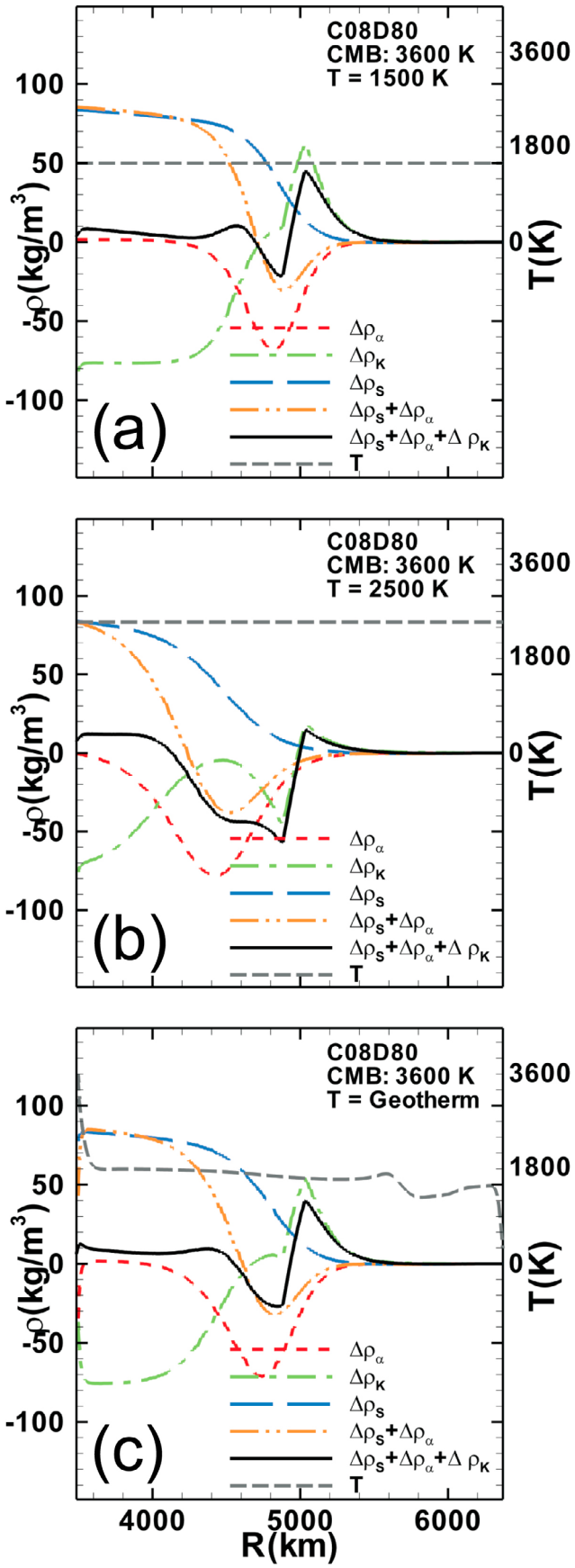

Figure 5. Depth (pressure) dependence of the density anomalies in the models *C08D80* due to the spin crossover in the lower mantle as discussed in the section 4.2 for (a) a low temperature of 1500 K, (b) a high temperature of 2500 K, and (c) a sample mantle geotherm. The spin-induced anomaly in bulk modulus $\Delta\rho_K$ is a superposition of the bulk modulus anomalies in ferropericlase (Figure 1c) and perovskite weighted by 1/3 and 2/3 respectively as displayed in Figure 4. The model assumes no spin-induced anomalies in density and thermal expansivity components ($\Delta\rho_s$, $\Delta\rho_\alpha$) in the perovskite component of mantle mineralogy and the anomalies arising in ferropericlase component are based on Figures 1a and 1b (weighted by 1/3).

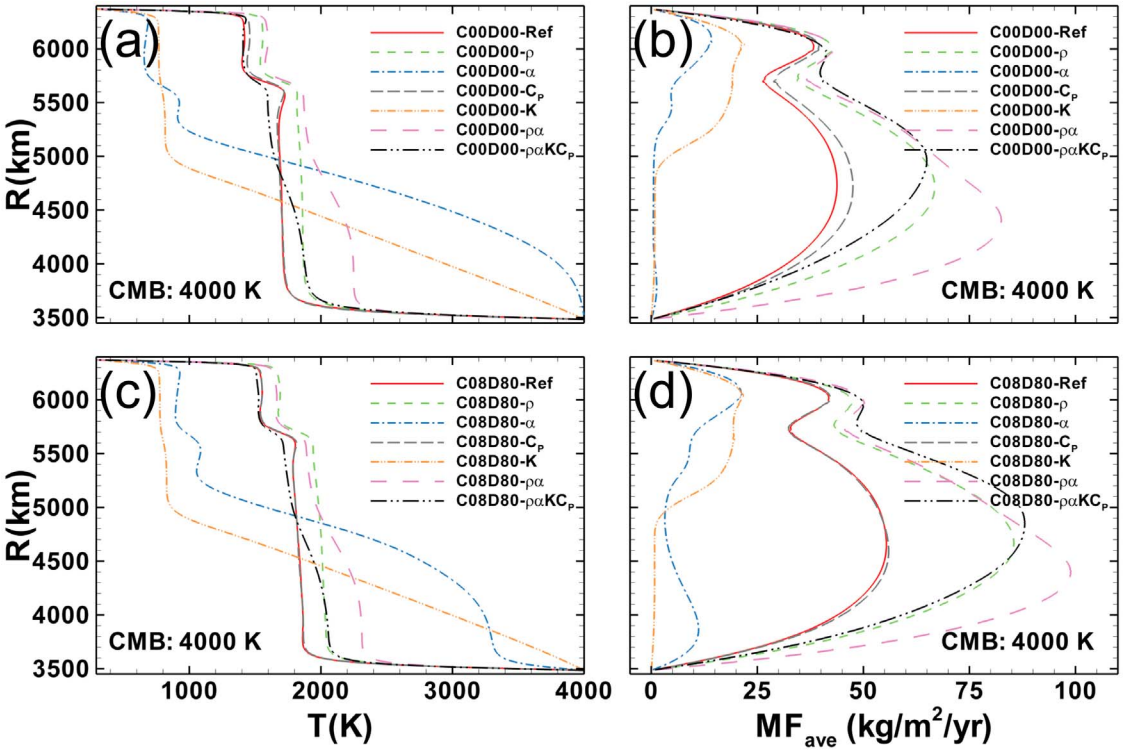

Figure 6. Results for the models with spin transition in both ferropericlase and perovskite as discussed in section 4.3. All models include the solid-solid phase transitions at 410 km and 660 km depths. (a) Mantle geotherms for the models with spin-induced anomalies described by the model names are compared with the reference model *C00D00 − Ref* (with no spin-induced anomalies). (b) Temporally averaged absolute radial mass flux profiles for the models described in Figure 6a. (c) The same as Figure 6a but the models further include Pv–pPv phase transition and are compared with the reference model *C08D80 − Ref* (with no spin-induced anomalies). (d) Temporally averaged absolute radial mass flux profiles for the models described in Figure 6c. In these models we have assumed quantitatively similar spin transition effects in thermodynamic properties of ferropericlase and perovskite with the weighting factors of 1/3 and 2/3 respectively, simply meaning that spin-induced anomalies incorporated in the models are those shown graphically by the Figure 1.

the absolute radial mass flux profiles at the sequence of times illustrated for these two models.

4.4. Iron Spin Crossover in Both Ferropericlase and Perovskite: An End-Member Model

[27] As mentioned earlier in this section, the density anomalies due to the spin-induced thermal expansivity anomaly and the spin-induced bulk modulus anomaly in ferropericlase are in competition. In final mantle convection model to be discussed herein we have assumed an extreme end-member example in which only the effect of the spin-induced density anomaly and spin-induced thermal expansivity anomaly are present, that is, a model incorporating $\Delta\rho_s + \Delta\rho_\alpha$ (i.e., excluding the bulk modulus anomaly) denoted by $C08D80 - \rho\alpha$ for which the CMB temperature is fixed to 4000 K. This will constitute an example in which the contributions arising from the spin-induced bulk modulus anomalies in ferropericlase and perovskite cancel a possibility that arises due to the opposite signs of these anomalies [*Wu et al.*, 2009; *Catalli et al.*, 2010]. Several time slices in the evolution of this model are shown in Figure 9. The first and second images at each snapshot, respectively, display the temperature and the total spin-induced density anomaly from which the laterally averaged spin-induced density anomaly has been subtracted (i.e., $\Delta\rho_s + \Delta\rho_\alpha - \overline{(\Delta\rho_s + \Delta\rho_\alpha)}$). The first snapshot reveals the presence of a stagnating mantle avalanche [*Peltier and Solheim*, 1992; *Solheim and Peltier*, 1994a, 1994b] at a depth of approximately 1800 km, one that was initially triggered at the 660 km phase boundary about 50 Myr earlier (not shown). The density anomaly field reveals that the avalanche induced volume of cold material has developed positive buoyancy due to the presence of the spin transition above the 1800 km depth horizon. Below this horizon there is a hot layer which has also acquired spin-induced positive buoyancy and which further assists in preventing the cold downwelling from penetrating through the 1800 km depth horizon.

[28] The frames in Figure 9b reveal a gradual penetration of the mantle flow into the lower midmantle which is followed by a sudden and vigorous flow penetration in the third snapshot which we will refer to as a spin-induced midmantle avalanche (SIMMA) event. The density anomalies depicted in the second image of each snapshot explicitly demonstrate that as long as the downwelling has not passed through a horizon determined by the minimum of the $\Delta\rho_s + \Delta\rho_\alpha$ curve in the transition zone (Figure 2) the flow has a positive buoyancy (compared to the lateral average). Once the flow

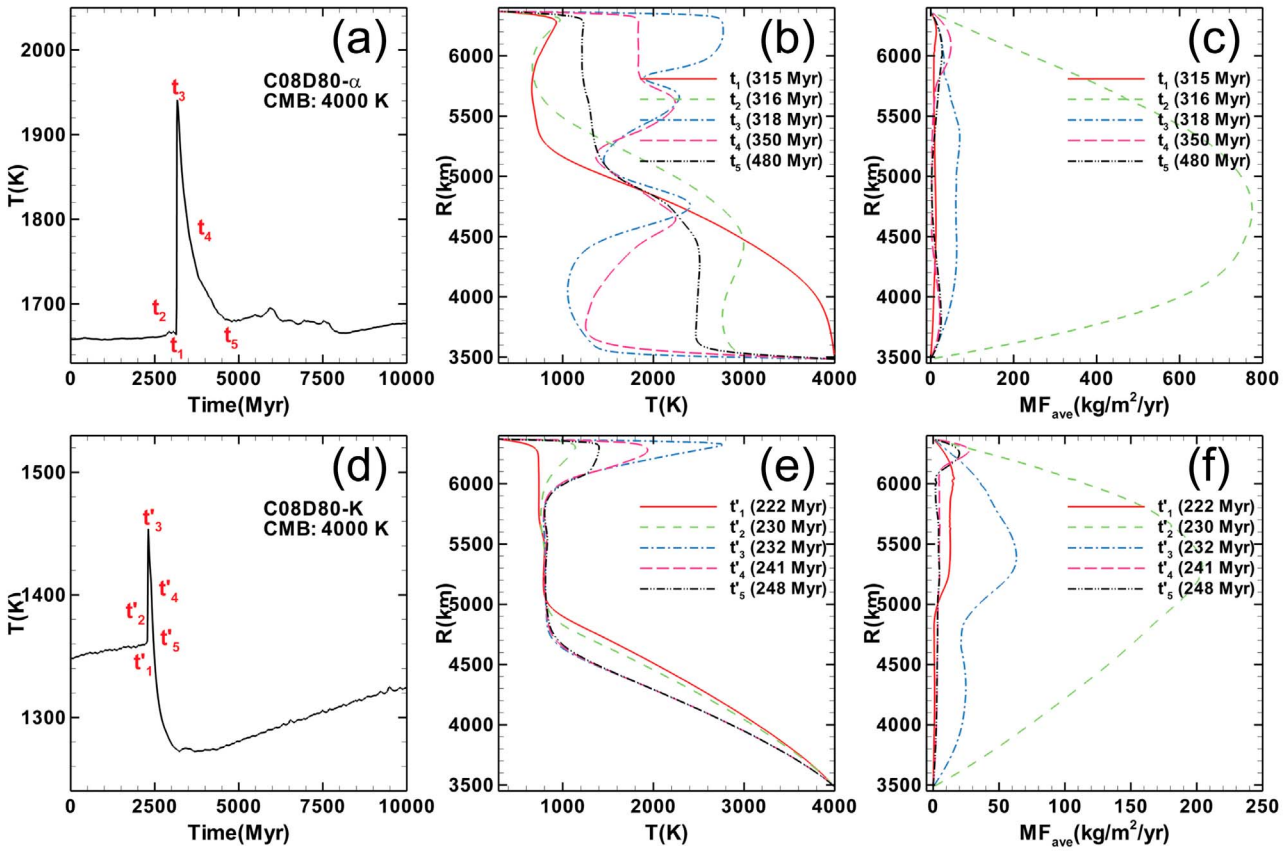

Figure 7. (a) The mean mantle temperature time series, (b) the geotherms and (c) the absolute radial mass flux profiles corresponding to the times indicated by t_1–t_5 for the model *C08D80 − α* (the model in which all spin-induced property changes are ignored except for the thermal expansivity). (d) The mean mantle temperature time series, (e) the geotherms and (f) the absolute radial mass flux profiles corresponding to the times indicated by t_1'–t_5' for the model *C08D80 − K* (the model in which all spin-induced property changes are ignored except for the bulk modulus).

penetrates through this horizon, however, it gains negative buoyancy which accelerates the downwelling flow which is the mechanism responsible for the SIMMA event. The remaining snapshots in Figure 9 display consecutive snapshots of this spin-induced mantle avalanche which explicitly show that, as the cold downwelling penetrates into the lower half of the lower mantle, depending on the pressure and temperature regime, the avalanche becomes denser than horizontally averaged mantle material. In a more realistic case that spin-induced bulk modulus anomaly of unknown magnitude will also be present and depending on the strength and sign of this anomaly, the SIMMA effect will weaken or completely disappear as was found to be the case in the present analyses when all spin-induced anomalies were included.

5. Conclusions

[29] For several decades the issue of the style of mantle mixing has been a primary focus of research in large scale geodynamics. The thermodynamic properties of lowermost mantle mineralogy are of fundamental importance in providing an adequate assessment of the spatiotemporal characteristics of the mantle general circulation. Only in recent years have the capabilities of high-pressure mineral physics experiments sufficiently improved to enable the development of fundamental new insights. Previous numerical modeling results therefore relied upon theoretical arguments or extrapolations based upon observed material properties under low P-T conditions. The impacts upon the physical properties of minerals under the extreme conditions of the deep mantle are important for the understanding of a wide range of Earth observations including data from the subfields of seismology, geochemistry, and geodynamics [*Gaffney and Anderson*, 1973; *Burns*, 1993]. The evolution of the planet itself, as this is controlled by the convection mediated rate of cooling, is strongly influenced by these physical properties. Under realistic mantle conditions it has now been clearly established that the spin state of iron may change from a high spin state to a lower spin state at a depth significantly below the 660 km seismic discontinuity. This HS-LS crossover in iron-bearing minerals may have significant impacts on the macroscopic physical properties of mantle minerals. Using an axisymmetric control volume based numerical model, we have investigated the possible effects of the iron spin crossover in mantle minerals on the convection process. In contrast to previous studies [e.g., *Bower et al.*, 2009] our study provides a detailed analysis of the spin-induced anomaly components

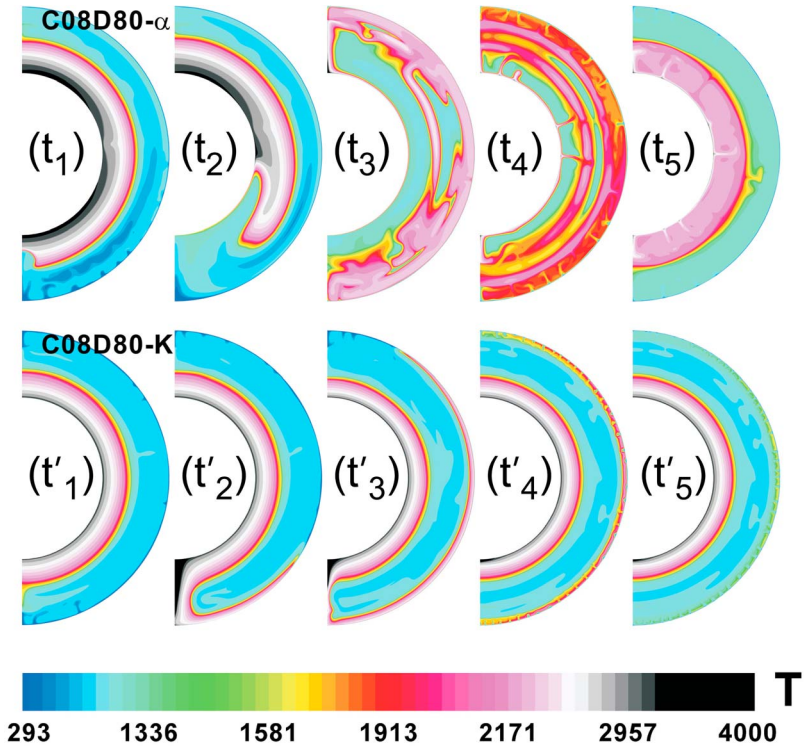

Figure 8. Snapshots of the temperature fields for the model *C08D80 − α* and *C08D80 − K* corresponding to the evolution times indicated in Figure 7.

and the influence of their strengths in the two main constituent minerals of the lower mantle. Our numerical results demonstrate that the spin crossover enhances the vigor of mixing in the lower mantle. The dominant effect of the spin crossover is to amplify the influence of the exothermic Pv–pPv phase transition in the further destabilization of mantle plumes [*Bower et al.*, 2009; *Shahnas and Peltier*, 2010] that originate in thermal instabilities near the CMB [*Matyska and Yuen*, 2006]. This is due to the fact that the net contribution of the sum of the spin-induced anomalies to the density enhances the buoyancy of mantle plumes.

[30] The existence of this transition also increases the density of cold downwellings in the lower levels of the mid mantle (higher pressures). Inspection of Figure 2a, reveals that a downgoing cold anomaly crossing the horizon at ~900 km depth begins to gain more negative buoyancy. From this depth to about 1600 km depth where the negative buoyancy achieves its maximum expression, the cold anomaly is accelerated (compared to a reference model which is assumed to be fully in the HS state). Below this depth there is a deceleration of the downwelling over a distance of approximately 300 km, following which the anomalous material is once again slightly accelerated (below 1900 km depth). Similarly, Figure 2b reveals that below the depth of 1900 km there is acceleration (compared to the reference model which is assumed to be fully in the HS state) of rising hot plumes. After this horizon is breached the buoyancy of the rising plumes is reduced between 1900 km and 1600 km depth. Above the 1600 km depth horizon hot rising plumes are accelerated once more.

[31] In the models for which the magnitude of the total density anomaly is sufficiently high (a state that would require that a similar spin transition also exists in perovskite or in which the magnitude of the anomalies in ferropericlase were higher than estimated here), and the net spin-induced bulk modulus anomaly is absent, the positive buoyancy experienced by descending mantle material may produce flow stagnation at a midmantle horizon, thereby preventing an avalanche that originates at the 660 km phase boundary from penetrating into the lowermost mantle. Such stagnation may continue for tens of millions of years until a sufficient degree of instability is established that a second avalanche (SIMMA) develops. In order for this phenomenon to occur, however, requires the absence of the spin-induced bulk modulus anomaly or at least a significant reduction in its strength. Although the contribution of a reduced spin-induced bulk modulus anomaly may diminish such SIMMA events the total spin-induced density anomaly may nevertheless slow descent of the downwellings below the endothermic and mid mantle horizons. This physical process could provide a dynamical explanation for the midmantle thermal anomalies that have been imaged tomographically below India and Tibet, as described by *Van der Voo et al.* [1999]. The shallow depth of the more northern of the cold thermal anomalies was interpreted by *Van der Voo et al.* [1999] to be the remnant of a cold slab from a fossil subduction zone which was terminated about 140 My ago [*Besse and Courtillot*, 1988]. Even with a viscosity increase of up to a factor of 65 across the mantle, *Jarvis and Lowman* [2005] were unable to account for this shallow anomaly on the basis of this suggestion. The possible spin transition–induced stagnation of mantle flow above

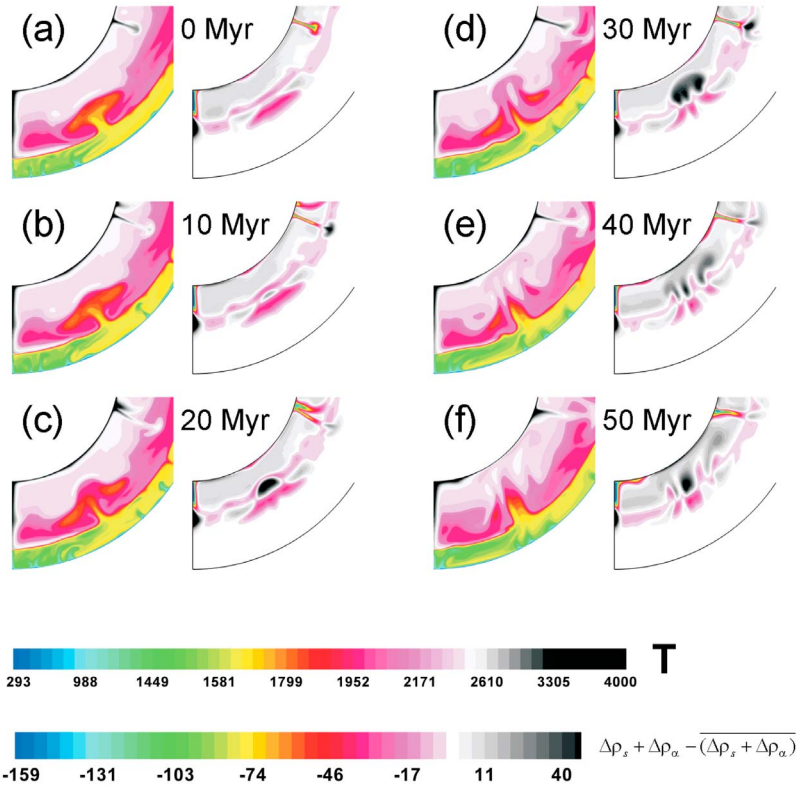

Figure 9. Snapshots of the spin-induced midmantle avalanche (SIMMA) event in the model *C08D80* − $\rho\alpha$ (CMB at 4000 K) described in section 4.4 in 10 Myr intervals. The first and second images at each snapshot show the temperature and spin-induced anomaly of $\Delta\rho_s + \Delta\rho_\alpha$ form which the laterally averaged anomalies have been subtracted at each grid point (i.e., $\Delta\rho_s + \Delta\rho_\alpha - \overline{(\Delta\rho_s + \Delta\rho_\alpha)}$) respectively.

the mid mantle horizon could provide an alternative explanation of the time delay required to explain this observation in terms of a fossil slab without the necessity of appealing to an extremely sharp increase of viscosity at midmantle depth. Although an increase of viscosity in this range of depths is inferred on the basis of the analysis of glacial isostatic adjustment observations [*Peltier and Drummond*, 2010], the actual increase has been shown to be modest.

[32] Figure 10 displays the laterally averaged spin-induced density variations (the total impact caused by the different components of the spin-induced anomalies) as deviations from the PREM density profile [*Dziewonski and Anderson*, 1981] for the different models discussed in section 4. Except for the density anomalies A–D discussed in section 4.1 and the density anomaly E discussed in section 4.2, the other density anomalies F and G discussed in section 4.3, and anomaly H discussed in section 4.4 as an end-member, are far from the PREM "constraint." The total density anomalies A–D, which represent the models in which we assume a spin transition to occur only in the ferropericlase component of the mineralogy (section 4.1), differ by at most 1.8% from the PREM density profile. This reduces to about 1.3% (−0.55%, +0.82%) for the E density anomaly (section 4.2), which represents the anomaly in the models in which, in addition to the spin-induced anomalies in ferropericlase [*Wu et al.*, 2009], we have considered the impact of a spin-induced anomaly in the bulk modulus in perovskite [*Catalli et al.*, 2010]. The density anomaly variation in the case of the end-member model discussed in section 4.4 is in the range of −2.2% and +4.5%. The higher positive deviation of this discrepancy is related to the fact that in this model we have assumed a similar spin-induced density anomaly in perovskite to that assumed for ferropericlase which is most probably an exaggeration. The lower strength of the spin-induced density anomaly in perovskite will decrease this deviation. Assuming no density anomaly in perovskite in this model (that is, spin-induced density and thermal expansivity anomalies in ferropericlase and only a spin-induced thermal expansivity anomaly in perovskite) will produce a density deviation curve similar to the one shown in anomaly I. Based on the trade off between the strength of the spin-induced thermodynamic property components in ferropericlase and perovskite, the discrepancy curve may vary approximately between the density anomaly curves E and I. Although the location of the minimum in the density anomaly may vary with the strength of anomaly components in the ferropericlase and perovskite components, this minimum seems to persist meaning that upwelling mantle plumes will experience deceleration when crossing the horizon determined by this minimum in the density anomaly.

[33] The seismologically derived Earth model PREM has provided limits on the density, pressure and elastic properties of the Earth's interior; however, the composition and the thermal structure of the Earth are still imperfectly constrained. For example *Ricolleau et al.* [2009] argue that, in order to match their measured density profile for a pyrolite mantle composition to PREM, the temperature at the top of

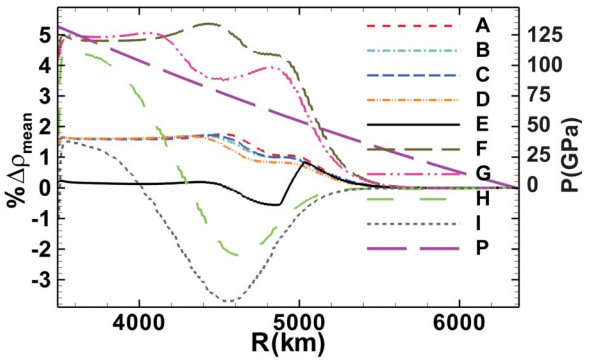

Figure 10. Deviations of the total spin-induced density anomalies form the laterally averaged density profile of PREM. The total density anomalies in the models in which only the spin-induced anomalies in ferropericlase have been considered: $C00D00 - \rho\alpha KC_P$ with the CMB temperature of 3600 K (A anomaly), $C08D80 - \rho\alpha KC_P$ with the CMB temperature of 3600 K (B anomaly), $C00D00 - \rho\alpha KC_P$ with the CMB temperature of 4000 K (C anomaly), $C08D80 - \rho\alpha KC_P$ with the CMB temperature of 4000 K (D anomaly) (section 4.1). The total density anomaly in the model in which further to the spin-induced anomalies in the ferropericlase we have considered the impact of the spin-induced anomaly in bulk modulus in perovskite: $C08D80 - \rho\alpha KC_P$ with the CMB temperature of 3600 K (E anomaly) (section 4.2). The total density anomalies in the models in which we have considered similar spin-induced anomalies both in ferropericlase and perovskite: $C00D00 - \rho\alpha KC_P$ with the CMB temperature of 4000 K (F anomaly), $C08D80 - \rho\alpha KC_P$ with the CMB temperature of 4000 K (G anomaly) (section 4.3). The total density anomaly in the end-member model in which we have investigated the overall impacts of the similar spin-induced anomalies in only density and thermal expansivity in both ferropericlase and perovskite: $C08D80 - \rho\alpha KC_P$ with the CMB temperature of 4000 K (H anomaly) (section 4.4). I anomaly displays the same impact as H anomaly except for the fact that in this case we have only considered the anomaly in thermal expansivity in perovskite excluding the density anomaly in this component of mineralogy. The mantle pressure (P) has been displayed by very long dashed line in GPa.

lower mantle has to be ~1500 ± 60 K which is ~400 K lower than the expected temperature at 660 km depth [e.g., *Hirose*, 2002] with a superadiabatic geotherm of gradient 0.60 K/km through the lower mantle. Their measured density for a peridotite mantle along the geotherm shows significant mismatch (2%) with the Preliminary Reference Earth Model (PREM) derived from seismic observations which may call for a reevaluation of the assumptions and uncertainties of PREM. Our inferred adjustments to the PREM density profile generally lie within this 2% constraint provided by the most recent high-pressure mineral physics measurements. The tentative conclusions in this paper concerning the impact of the iron spin transition on mantle mixing have relied entirely upon the available high-pressure experimental data for the ferropericlase and perovskite components of lower mantle mineralogy. Although that for ferropericlase is reasonably complete that for perovskite is not. In this circumstance the SIMMA events we have discussed must be considered speculative. The analyses presented nevertheless serve the purpose of reinforcing the important role that the anomalous physical properties associated with the spin transition may play in mantle dynamics.

[34] **Acknowledgments.** The computations on which the paper is based were performed on the SciNet facility for High Performance Computation at the University of Toronto which is a component of the Compute Canada HPC platform. Additional support was provided by NSERC Discovery grant A9627 to W.R.P.

References

Badro, J., G. Fiquet, F. Guyot, J.-P. Rueff, V. V. Struzhkin, G. Vanko, and G. Monaco (2003), Iron partitioning in Earth's mantle: Toward a deep lower mantle discontinuity, *Science*, *300*, 789–791.

Badro, J., J.-P. Rueff, G. Vanko, G. Monaco, G. Fiquet, and F. Guyot (2004), Electronic transitions in perovskite: Possible nonconvecting layers in the lower mantle, *Science*, *305*, 383–386, doi:10.1126/science.1098840.

Badro, J., G. Fiquet, and F. Guyot (2005), Thermochemical state of the lower mantle: New insights from mineral physics, in *Earth's Deep Mantle: Structure, Composition, and Evolution*, *Geophys. Monogr. Ser.*, vol. 160, edited by R. D. van der Hilst et al., pp. 241–260, AGU, Washington, D. C.

Bengtson, A., J. Li, and D. Morgan (2009), Mössbauer modeling to interpret the spin state of iron in (Mg, Fe)SiO_3 perovskite, *Geophys. Res. Lett.*, *36*, L15301, doi:10.1029/2009GL038340.

Besse, J., and V. Courtillot (1988), Paleogeographic maps of the continents bordering the Indian Ocean since the Early Jurassic, *J. Geophys. Res.*, *93*, 11,791–11,808, doi:10.1029/JB093iB10p11791.

Boehler, R. (1992), Melting of the Fe-FeO and the Fe-FeS systems at high pressure: Constraints on core temperatures, *Earth Planet. Sci. Lett.*, *111*, 217–227, doi:10.1016/0012-821X(92)90180-4.

Bower, D. J., M. Gurnis, J. M. Jackson, and W. Sturhahn (2009), Enhanced convection and fast plumes in the lower mantle induced by the spin transition in ferropericlase, *Geophys. Res. Lett.*, *36*, L10306, doi:10.1029/2009GL037706.

Burns, R. G. (1993), *Mineralogical Application of Crystal Field Theory*, Cambridge Univ. Press, Cambridge, U. K, doi:10.1017/CBO9780511524899.

Butler, S. L., and W. R. Peltier (2002), Thermal evolution of Earth: Models with time-dependent layering of mantle convection which satisfy the Urey ratio constraint, *J. Geophys. Res.*, *107*(B6), 2109, doi:10.1029/2000JB000018.

Catalli, K., S.-H. Shim, P. Dera, V. B. Prakapenka, J. Zhao, W. Sturhahn, Y. Xiao, P. Chow, H. Cynn, and W. Evans (2009), Volume collapse of iron, aluminum-bearing perovskite at mid-lower mantle pressures, *Eos Trans. AGU*, *90*(52), Fall Meet. Suppl., Abstract DI12A–04C.

Catalli, K., S.-H. Shim, V. B. Prakapenka, J. Zhao, W. Sturhahn, P. Chow, Y. Xiao, H. Liu, H. Cynn, and W. J. Evans (2010), Spin transition in ferric iron in $MgSiO_3$ perovskite and its effect on elastic properties, *Earth Planet. Sci. Lett.*, *289*, 68–75.

Cohen, R. E., I. I. Mazin, and D. Isaak (1997), Magnetic collapse in transition metal oxides at high pressure: Implications for the Earth, *Science*, *275*, 654–657, doi:10.1126/science.275.5300.654.

Crowhurst, J. C., J. M. Brown, A. F. Goncharov, and S. D. Jacobsen (2008), Elasticity of (Mg, Fe)O through the spin transition of iron in the lower mantle, *Science*, *319*, 451–453, doi:10.1126/science.1149606.

Dziewonski, A., and D. Anderson (1981), Preliminary reference Earth model, *Phys. Earth Planet. Inter.*, *25*, 297–356, doi:10.1016/0031-9201(81)90046-7.

Fei, Y. (1995), Thermal expansion, in *Mineral Physics and Crystallography: A Handbook of Physical Constants*, *AGU Ref. Shelf*, vol. 2, edited by T. J. Ahrens, pp. 64–97, AGU, Washington, D. C.

Fei, Y., L. Zhang, A. Corgne, H. Watson, A. Ricolleau, Y. Meng, and V. Prakapenka (2007), Spin transition and equations of state of (Mg, Fe)O solid solutions, *Geophys. Res. Lett.*, *34*, L17307, doi:10.1029/2007GL030712.

Fyfe, W. S. (1960), The possibility of d-electron coupling in olivine at high pressures, *Geochim. Cosmochim. Acta*, *19*, 141–143, doi:10.1016/0016-7037(60)90046-6.

Gaffney, E. S., and D. L. Anderson (1973), Effect of Low-Spin Fe^{2+} on the composition of the lower mantle, *J. Geophys. Res.*, *78*, 7005–7014, doi:10.1029/JB078i029p07005.

Goncharov, A. F., V. V. Struzhkin, and S. D. Jacobsen (2006), Reduced radiative conductivity of low-spin (Mg, Fe)O in the lower mantle, *Science*, *312*, 1205–1208, doi:10.1126/science.1125622.

Hirose, K. (2002), Phase transitions in pyrolitic mantle around 670-km depth: Implications for upwelling of plumes from the lower mantle, *J. Geophys. Res.*, *107*(B4), 2078, doi:10.1029/2001JB000597.

Hofmeister, A. M. (1999), Mantle values of thermal conductivity and the geotherm from phonon lifetimes, *Science*, *283*, 1699–1706, doi:10.1126/science.283.5408.1699.

Hofmeister, A. M. (2006), Is low-spin Fe^{2+} present in Earth's mantle?, *Earth Planet. Sci. Lett.*, *243*, 44–52, doi:10.1016/j.epsl.2005.12.013.

Hsu, H., K. Umemoto, R. M. Wentzcovitch, and P. Blaha (2010), Spin states and hyperfine interactions of iron in (Mg, Fe)SiO_3 perovskite under pressure, *Earth Planet. Sci. Lett.*, *294*, 19–26, doi:10.1016/j.epsl.2010.02.031.

Jackson, J. M., W. Sturhahn, G. Shen, J. Zhao, and M. Y. Hu (2005), A synchrotron Mössbauer spectroscopy study of (Mg, Fe)SiO_3 perovskite up to 120 GPa, *Am. Mineral.*, *90*, 199–205, doi:10.2138/am.2005.1633.

Jarvis, G. T., and J. P. Lowman (2005), Sinking slabs below fossil subduction zones, *Phys. Earth Planet. Inter.*, *152*, 103–115, doi:10.1016/j.pepi.2005.05.002.

Kumar, M. (2000), Equation of state and bulk modulus under the effect of high pressure-high temperature, *Phys. Chem. Miner.*, *27*, 650–655, doi:10.1007/s002690000118.

Li, J., V. V. Struzhkin, H.-K. Mao, J. Shu, R. J. Hemley, Y. Fei, B. Mysen, P. Dera, V. Prakapenka, and G. Shen (2004), Electronic spin state of iron in lower mantle perovskite, *Proc. Natl. Acad. Sci. U. S. A.*, *101*, 14,027–14,030, doi:10.1073/pnas.0405804101.

Li, J., W. Sturhahn, J. M. Jackson, V. V. Struzhkin, J. F. Lin, J. Zhao, H. K. Mao, and G. Shen (2006), Pressure effect on the electronic structure of iron in (Mg, Fe)(Si, Al)O_3 perovskite: A combined synchrotron Mössbauer and X-ray emission spectroscopy study up to 100 GPa, *Phys. Chem. Miner.*, *33*, 575–585, doi:10.1007/s00269-006-0105-y.

Lin, J. F., and T. Tsuchiya (2008), Spin transition of iron in the Earth's lower mantle, *Phys. Earth Planet. Inter.*, *170*, 248–259, doi:10.1016/j.pepi.2008.01.005.

Lin, J. F., V. V. Struzhkin, S. D. Jacobsen, M. Y. Hu, P. Chow, J. Kung, H. Z. Liu, H. K. Mao, and R. J. Hemley (2005), Spin transition of iron in magnesiowustite in the Earth's lower mantle, *Nature*, *436*, 377–380, doi:10.1038/nature03825.

Lin, J. F., G. Vankó, S. D. Jacobsen, V. Iota, V. V. Struzhkin, V. B. Prakapenka, A. Kuznetsov, and C. S. Yoo (2007), Spin transition zone in Earth's lower mantle, *Science*, *317*, 1740–1743, doi:10.1126/science. 1144997.

Lin, J. F., et al. (2008), Intermediate-spin ferrous iron in lowermost mantle post-perovskite and perovskite, *Nat. Geosci.*, *1*, 688–691, doi:10.1038/ngeo310.

Lundin, S., K. Catalli, J. Santillán, S.-H. Shim, V. B. Prakapenka, M. Kunz, and Y. Meng (2008), Effect of Fe on the equation of state of mantle silicate perovskite over 1 Mbar, *Phys. Earth Planet. Inter.*, *168*, 97–102, doi:10.1016/j.pepi.2008.05.002.

Matyska, C., and D. A. Yuen (2006), Lower mantle dynamics with the post-perovskite phase change, radiative thermal conductivity, temperature- and depth-dependent viscosity, *Phys. Earth Planet. Inter.*, *154*, 196–207, doi:10.1016/j.pepi.2005.10.001.

McCammon, C., I. Kantor, O. Narygina, J. Rouquette, U. Ponkratz, I. Sergueev, M. Mezouar, V. Prakapenka, and L. Dubrovinsky (2008), Stable intermediate-spin ferrous iron in lower-mantle perovskite, *Nat. Geosci.*, *1*, 684–687.

Murakami, M., K. Hirose, K. Kawamura, N. Sata, and Y. Ohishi (2004), post-perovskite phase transition in $MgSiO_3$, *Science*, *304*, 855–858, doi:10.1126/science.1095932.

Oganov, A., and A. R. Ono (2004), Theoretical and experimental evidence for a post-perovskite phase of $MgSiO_3$ in Earth's D″ layer, *Nature*, *430*, 445–448, doi:10.1038/nature02701.

Patankar, S. V. (1980), *Numerical Heat Transfer and Fluid Flow*, McGraw-Hill, New York.

Patankar, S. V., and D. B. Spalding (1972), A calculation procedure for heat, mass and momentum transfer in three-dimensional parabolic flows, *Int. J. Heat Mass Transfer*, *15*, 1787–1806, doi:10.1016/0017-9310(72)90054-3.

Peltier, W. R. (1998), Postglacial variations in the level of the sea: Implications for climate dynamics and solid-Earth geophysics, *Rev. Geophys.*, *36*(4), 603–689, doi:10.1029/98RG02638.

Peltier, W. R., and R. Drummond (2010), Deepest mantle viscosity: Constraints from Earth rotation anomalies, *Geophys. Res. Lett.*, *37*, L12304, doi:10.1029/2010GL043219.

Peltier, W. R., and L. P. Solheim (1992), Mantle phase transitions and layered chaotic convection, *Geophys. Res. Lett.*, *19*, 321–324, doi:10.1029/91GL02951.

Peltier, W. R., S. Butler, and L. P. Solheim (1997), The influence of phase transformation on mantle mixing and plate tectonics, in *Earth*'s *Deep Interior*, edited by D. J. Crossley, pp. 405–430, Gordon and Breach, Amsterdam.

Ricolleau, A., et al. (2009), Density profile of pyrolite under the lower mantle conditions, *Geophys. Res. Lett.*, *36*, L06302, doi:10.1029/2008GL036759.

Ringwood, A. E. (1982), Phase transformations and differentiation in subducted lithosphere: Implications for mantle dynamics basalt petrogenesis and crustal evolution, *J. Geol.*, *90*, 611–643, doi:10.1086/628721.

Schmeling, H., G. Marquart, and T. Ruedas (2003), Pressure and temperature-dependent thermal expansivity and the effect on mantle convection and surface observables, *Geophys. J. Int.*, *154*, 224–229, doi:10.1046/j.1365-246X.2003.01949.x.

Shahnas, M. H., and W. R. Peltier (2010), Layered convection and the impacts of the perovskite-post perovskite phase transition on mantle dynamics under isochemical conditions, J, *J. Geophys. Res.*, *115*, B11408, doi:10.1029/2009JB007199.

Shannon, R. D., and C. T. Prewitt (1969), Effective ionic radii in oxides and fluorides, Acta Crystallogr., *Sect. B Struct. Crystallogr. Cryst. Chem.*, *25*, 925–946, doi:10.1107/S0567740869003220.

Sherman, D. M. (1988), Structural and Magnetic Phase Transitions in Minerals, *Adv. in Phys. Geochem.*, vol. *7*, edited by S. Ghose, J. M. D. Coey, and E. Salje, pp. 113–128, Springer, New York.

Sherman, D. M. (1991), The high-pressure electronic structure of magnesiowustite (Mg, Fe)O: Applications to the physics and chemistry of the lower mantle, *J. Geophys. Res.*, *96*, 14,299–14,312, doi:10.1029/91JB01202.

Solheim, L. P., and W. R. Peltier (1993), Mantle phase transitions and layered convection, *Can. J. Earth Sci.*, *30*(5), 881–892, doi:10.1139/e93-073.

Solheim, L. P., and W. R. Peltier (1994a), Avalanche effects in phase transition modulated thermal convection: A model of Earth's mantle, *J. Geophys. Res.*, *99*, 6997–7018, doi:10.1029/93JB02168.

Solheim, L. P., and W. R. Peltier (1994b), Phase boundary deflections at 660-km depth and episodically layered isochemical convection in the mantle, *J. Geophys. Res.*, *99*, 15,861–15,875, doi:10.1029/94JB00730.

Speziale, S., A. Milner, V. E. Lee, S. M. Clark, M. P. Pasternak, and R. Jeanloz (2005), Iron spin transition in Earth's mantle, *Proc. Natl. Acad. Sci. U. S. A.*, *102*, 17,918–17,922, doi:10.1073/pnas.0508919102.

Sturhahn, W., J. M. Jackson, and J. F. Lin (2005), The spin state of iron in minerals of Earth's lower mantle, *Geophys. Res. Lett.*, *32*, L12307, doi:10.1029/2005GL022802.

Tsuchiya, T., R. M. Wentzcovitch, C. R. S. da Silva, and S. de Gironcoli (2006), Spin transition in magnesiowustite in Earth's lower mantle, *Phys. Rev. Lett.*, *96*, 198501, doi:10.1103/PhysRevLett.96.198501.

Tsuchiya, T., J. Tsuchiya, K. Umemoto, and R. M. Wentzcovitch (2004), Phase transition in $MgSiO_3$-perovskite in the Earth's lower mantle, *Earth Planet. Sci. Lett.*, *224*, 241–248, doi:10.1016/j.epsl.2004.05.017.

van den Berg, A. P., D. A. Yuen, and J. R. Allwardt (2002), Non-linear effects from variable thermal conductivity and mantle internal heating: Implications for massive melting and secular cooling of the mantle, *Phys. Earth Planet. Inter.*, *129*, 359–375.

Van der Voo, R., W. Spakman, and H. Bijwaard (1999), Tethyan subducted slabs under India, *Earth Planet. Sci. Lett.*, *171*, 7–20, doi:10.1016/S0012-821X(99)00131-4.

Wentzcovitch, R. M., J. F. Justo, Z. Wu, C. R. S. da Silva, D. Yuen, and D. Kohlstedt (2009), Anomalous compressibility of ferropericlase throughout the iron spin crossover, *Proc. Natl. Acad. Sci. U. S. A.*, *106*, 8447–8452.

Wu, Z., J. F. Justo, C. R. S. da Silva, S. de Gironcoli, and R. M. Wentzcovitch (2009), Anomalous thermodynamic properties in ferropericlase throughout its spin crossover transition, *Phys. Rev.*, *80*, 014409, doi:10.1103/PhysRevB.80.014409.

Zhang, F., and A. Oganov (2006), Valence state and spin transitions of iron in Earth's mantle silicates, *Earth Planet. Sci. Lett.*, *249*, 436–443, doi:10.1016/j.epsl.2006.07.023.

W. R. Peltier and M. H. Shahnas, Department of Physics, University of Toronto, 60 St. George St., Toronto, ON M5S 1A7, Canada. (shahnas@atmosp.physics.utoronto.ca; peltier@atmosp.physics.utoronto.ca)

R. Wentzcovitch, Minnesota Supercomputing Institute, University of Minnesota, Minneapolis, MN 55455, USA. (wentz002@umn.edu)

Z. Wu, Collaboratory for Advanced Computing and Simulations, University of Southern California, Los Angeles, CA 90089-0242, USA. (zqwu00@gmail.com)